A multi-scale assessment of the flow mechanics of polymer support fluids in granular soils

Si Suo[1,2], Mingliang Qu[3], Yongxin Wang[4], Stephan A Jefferis[5], Martin J Blunt[6], and Catherine O'Sullivan[7]

[1]Dept. of Civil and Environmental Engineering, Imperial College London, London SW7 2BU, UK. Email: s.suo@imperial.ac.uk

[2]Dept. of Earth Science and Engineering, Imperial College London, London SW7 2BP, UK.

[3]Dept. of Earth Science and Engineering, Imperial College London, London SW7 2BP, UK. Email: m.qu@imperial.ac.uk

[4]Dept. of Civil and Environmental Engineering, Imperial College London, London SW7 2BU, UK. Email: yongxin.wang22@imperial.ac.uk

[5]Environmental Geotechnics Ltd, St Mary's Grove, Adderbury, Banbury, UK. Email: egl@environmentalgeotechnics.com

[6]Dept. of Earth Science and Engineering, Imperial College London, London SW7 2BP, UK. Email: m.blunt@imperial.ac.uk

[7]Dept. of Civil and Environmental Engineering, Imperial College London, London SW7 2BU, UK. Email: cath.osullivan@imperial.ac.uk

ABSTRACT

Polymer fluids present a number of advantages over bentonite-based alternatives for excavation support. Much is still to be learned about the permeation of these non-Newtonian fluids in soils and especially more permeable soils and there is uncertainty around the support forces imparted to the soil. This study develops a numerical framework based on a pore-network modeling approach to quantify the grain drag forces induced by polymer flows in sand packings. The model

captures the shear-thinning rheology of polymer fluids and the emergent data reveal the distinct flow dynamics and their influence on grain-scale interactions. The shear-thinning rheology of these fluids amplifies flow heterogeneity, leading to a non-linear relationship between individual grain drag and the total applied pressure gradient if it exceeds a critical threshold. Implications of these fundamental observations for engineering practice are demonstrated through an example application to excavation support during diaphragm wall construction.

INTRODUCTION

In recent decades, polymer support fluids, i.e. aqueous solutions of partially hydrolyzed polyacrylamides (PHPAs or HPAMs), have emerged as a promising alternative to bentonite slurries to provide excavation support during the construction of bored piles, diaphragm walls, etc. (Lam and Jefferis 2014; Lam and Jefferis 2018; EFFC/DFI 2019), while water may be suitable but limited to low-permeability formations, e.g., clay soils (EFFC/DFI 2019). Compared to bentonite slurries, polymer fluids offer several advantages: they require less site infrastructure and lighter pumping equipment due to their lower density (close to that of water), and they are easier to dispose of after use. Despite these benefits, adoption of polymer fluids in the construction industry remains limited. One barrier to uptake is an incomplete understanding of polymer fluid permeation and its interactions with adjacent soils. This knowledge gap has led to occasional unsuccessful applications, fostering reluctance to rely on polymer fluids (Jefferis and Lam 2013).

The support mechanisms of polymer fluids differ fundamentally from those of bentonite slurries (e.g. Lam and Jefferis (2018)). Unlike bentonite slurries, polymer fluids do not form a filter cake on the excavation side walls. Instead, a pressure gradient drives their permeation into the soil adjacent to the excavation and the support provided by polymer fluids arises from drag forces exerted on the soil particles. At a macro-scale (continuum-scale) this means that a key objective must be to achieve a pressure drop close to the excavation face. Quantifying grain drag is relevant to a number of applications in geomechanics, e.g., internal erosion, sand production in wells and liquefaction. Consequently, numerous experimental and numerical studies have explored grain drag forces for groundwater and other Newtonian fluids with viscosities that do not vary with shear rate (Liu

et al. 2021; Climent et al. 2014; Salomon et al. 2024; Chareyre et al. 2012; Sanvitale et al. 2023). However, findings from these studies cannot be directly transferred to polymer fluids because they exhibit a shear-thinning behavior so that their apparent viscosity decreases with increasing fluid shear rate. Polymer fluid permeation in porous geomaterials has been considered in other applications including enhanced oil recovery in petroleum engineering (Sorbie 1991; Kumar et al. 2024). These applications generally do not require consideration of the support provided to the solid phase by the permeating fluid. While we have developed a fundamental understanding of how the non-Newtonian rheology affects polymer fluid flow in porous media (Suo et al. 2025; Rodríguez de Castro et al. 2023), the specific influence of polymer rheology on grain drag forces and its implications for excavation support remain poorly understood.

The objectives of this study are threefold: (1) to quantify the grain drag forces induced by polymer flows in sand packings; (2) to explore the relationship between the applied pressure gradient and grain drag, particularly beyond the critical thresholds where non-Newtonian effects dominate; and (3) to link the grain-scale analysis to geotechnical design analyses.

As the individual grain drag in a packing cannot be directly measured in experiments, numerical approaches are needed. While direct numerical simulations (DNS) can provide a fully-resolved solution of the flow field and the grain drag accurately, their high computational cost limits their application to simulations with only a few grains. While more computationally efficient coupled unresolved computational fluid dynamics-discrete element method (CFD-DEM) simulations have been used successfully for water-sand interaction simulations in geomecahnics, an empirical drag model is required and the available models were developed for water only. Furthermore the fluid phase in CFD-DEM simulations is simulated using a mesh with grid cells larger than the particles. Pore-network modeling (PNM) is an alternative method that considers the essential pore-scale details rather than fully resolving the pore space and therefore can be extremely computationally efficient in comparison (Blunt et al. 2013; Blunt 2017; Morimoto et al. 2024).

To achieve the above objectives, this study develops a novel numerical framework incorporating PNM and a customized module for grain drag force calculations. This approach enables a systematic

investigation of the effects of polymer rheology, polymer properties, and sand characteristics on grain drag forces. The engineering relevance of the findings is demonstrated through a case study, providing insights for the rational design and risk mitigation for deep excavation support using polymer fluids.

PORE-NETWORK MODELING

Flow simulation

PNM simulates flow by simplifying the void space into a network of wide regions which are pores (network nodes), connected by edges which are throats or constrictions (network links) (Bryant and Blunt 1992; Morimoto et al. 2024).

The governing equation is expressed in terms of pore pressure and built upon mass conservation and the assumption that the pressure within each pore is constant:

$$\sum_{j=1}^{N_i} Q_{ij}(|\nabla P|_{ij}) = 0, \tag{1}$$

where N_i is the pore coordination number, i.e., the total number of throats connected to pore i; Q_{ij} is the volumetric flow rate through throat ij, connecting pores i and j, determined by its pressure gradient $|\nabla P|_{ij}$. Due to the non-Newtonian rheology of polymer fluids, the local conductance of each throat $Q_{ij}(|\nabla P|_{ij})$ is a non-linear function of the applied pressure gradient $|\nabla P|_{ij}$. In this study, the apparent viscosity of polymer fluids is modeled by a power law with two truncated limits (i.e. the upper and lower Newtonian plateaus) as shown in Fig. 1,

$$\mu = \max\{\mu_\infty,\ \min[\mu_0,\ \mu_0(\frac{\dot{\gamma}}{\dot{\gamma}_0})^{n-1}]\}, \tag{2}$$

where n is the power-law index; μ_0 and μ_∞ are the upper and lower bounds of μ, known as the zero-shear-rate and the infinite-shear-rate viscosities, which correspond to the two limits of the power-law range ($\dot{\gamma}_0,\ \dot{\gamma}_\infty$). The conductance model $Q_{ij}(|\nabla P|_{ij})$ and the iterative algorithm to solve Eq. 1 are detailed in Suo et al. (2025).

Sand packings and network extraction

Virtual sphere packings (VSPs) were adopted as digital models of real sand samples. By adjusting the particle size distribution (PSD) and porosity (ϕ), VSPs can represent a wide range of sands. In this study, typical reference sands, including Leighton Buzzard sands (LBS), (Taylor et al. 2017; Ejezie et al. 2021), Ottawa sands (OS) (Carey et al. 2020), and Toyoura sands (TS) (Yang and Sze 2011) were considered as summarised in Table 1. The sphere packing generation approach is detailed in (Suo et al. 2023). The intrinsic permeability K of each sand sample is calculated by the pore-network model.

Fig. 2 shows the workflow of the pore network extraction. To extract the network, the sphere packing is first voxelized to create a labeled 3D image, i.e., the pore space is marked zero, and each sphere is labeled by a unique positive integer. The grain drag calculation requires the identification of connections between each grain and its neighboring pores. Therefore, a bespoke dual-network extraction technique is employed. The extraction algorithm is based on the maximal ball method (Raeini et al. 2017; Dong and Blunt 2009). The maximal ball method finds the local largest inscribed sphere in each pore by determining the local maximum in the distance to the nearest solid. The center of the maximal ball defines the pore center, and the pore radius is the maximal ball, while the throats are the constricted regions between neighboring (connected) pores. The cross-sectional shapes of all throats are then classified as circular, triangular, or square based on their geometric properties (Valvatne and Blunt 2004). For the solid phase, a marker-based watershed algorithm (Qu et al. 2023) was employed to identify solid grains, with each grain represented as a solid node. At this stage, the interface area between the pore space and the solid phase can be measured using methods developed in (Qu et al. 2023; Qu et al. 2024). It is important to note that the coordinates of each voxel can be determined, and the drag force vector at each voxel also can be calculated.

Fluid-grain interaction force calculation

Once the network of pores and throats has been extracted, flow modeling can be performed (Suo et al. 2025). Based on the flow field, the fluid-grain interaction force $\mathbf{F}_t$ can be calculated by

considering its two components (Chareyre et al. 2012):

$$\mathbf{F}_\mathrm{t} = \mathbf{F}_\mathrm{p} + \mathbf{F}_\mathrm{v}, \tag{3}$$

where the form drag, $\mathbf{F}_\mathrm{p}$, arises from the fluid pressure normal to the grain surface; and the skin friction $\mathbf{F}_\mathrm{v}$, is induced by the viscous shear along the grain surface.

As schematically illustrated in Fig. 3(a), the form drag $\mathbf{F}_\mathrm{p}^i$ acting on grain i is calculated as a summation of the pore pressure force $\mathbf{F}_\mathrm{p}^{ij}$ from the N_P neighboring pores (1 to j). The interface between grain i and pore j is discretized into N_V voxels. The contribution of each voxel to $\mathbf{F}_\mathrm{p}^{ij}$ is calculated as $P^j A_\mathrm{V}^{ij} \mathbf{n}_\mathrm{V}^{ij}$, where P^j is the pressure in pore j, A_V^{ij} is the interfacial area and $\mathbf{n}_\mathrm{V}^{ij}$ is the normal vector from the voxel center to the grain center. Finally, $\mathbf{F}_\mathrm{p}^i$ is calculated using

$$\mathbf{F}_\mathrm{p}^i = \sum_{j=1}^{N_\mathrm{P}} \mathbf{F}_\mathrm{p}^{ij} = \sum_{j=1}^{N_\mathrm{P}} \sum_{k=1}^{N_\mathrm{V}} P^j A_\mathrm{V}^{jk} \mathbf{n}_\mathrm{V}^{jk}. \tag{4}$$

The viscous shear contribution is calculated based on the fact that in Stokes flow, the pressure drop along a throat is balanced by the viscous force (Chareyre et al. 2012). The total viscous force along the throat ij is estimated as

$$\mathbf{F}_\mathrm{v}^{\mathrm{total},ij} = (P^i - P^j) A_\mathrm{t}^{ij} \mathbf{n}_\mathrm{t}^{ij}, \tag{5}$$

where A_t^{ij} is the cross-sectional area and $\mathbf{n}_t^{ij}$ is the unit vector pointing from pore i to pore j. Then, we assume that the viscous force applied on the grain k is proportional to its interfacial area $A_\mathrm{g}^{\mathrm{k},ij}$ connected with pores i and j, as shown in Fig. 3(b). Thus, the skin friction $\mathbf{F}_\mathrm{v}^{k,ij}$ on grain k reads

$$\mathbf{F}_\mathrm{v}^{\mathrm{k},ij} = \mathbf{F}_\mathrm{v}^{\mathrm{total},ij} \frac{A_\mathrm{g}^{\mathrm{k},ij}}{\sum_{\mathrm{k}=1}^{N_\mathrm{g}} A_\mathrm{g}^{\mathrm{k},ij}}, \tag{6}$$

where N_g is the number of all grains forming the throat ij. The total skin friction $\mathbf{F}_\mathrm{v}^k$ on grain k is the summation of $\mathbf{F}_\mathrm{v}^{k,ij}$ by iterating all throats touching the grain k.

CALIBRATION, VERIFICATION AND VALIDATION

High-resolution direct numerical simulation (DNS) using computational fluid dynamics (CFD) is able to capture physically realistic flow fields (Sanvitale et al. 2023), and therefore can accurately calculate the fluid-solid interaction forces. Comparing with a DNS is an effective pathway not only to calibrate parameters in the PNM but more importantly to verify and quantitatively validate the newly proposed module of calculating grain drags.

Fully resolved DNS

The computational cost of a DNS is significant; so a relatively small VSP was generated to model the LBS sample named "Ejezie A" (Ejezie et al. 2021), (See Table 1). The results obtained from DNS are taken as a benchmark to investigate to what extent the PNM can reproduce the DNS data, confirm the conductance model is adequate, and determine the required voxel resolution for calculating the $\mathbf{F}_{\mathrm{p}}^{i}$ values in the PNM.

The DNS considered fully developed Stokes flow. The flow domain comprised 404 grains including 142 complete grains, as shown in Fig. 4. All grains were fixed in place, and a no-slip boundary condition was applied on the grain surface. The flow was directed along the z axis. A fixed-velocity boundary condition ($U_0 = 10^{-4}$ m/s) was imposed at the inlet ($z_{\max}$), while a zero-pressure boundary condition ($P = 0$ Pa) was imposed at the outlet ($z_{\min}$). On other boundaries, i.e., the front, back, left, and right planes, free-slip boundary conditions were imposed.

Following Taylor et al. (2016) and Sanvitale et al. (2023), we used the open-source CFD code OpenFOAM (https://www.openfoam.com/news/main-news/openfoam-v2106). The SIMPLE solver (Patankar and Spalding 1983) was employed to solve the steady Navier-Stokes equations for incompressible fluid flow. The body-fitted mesh was generated using SnappyHexMesh following Mačak et al. (2025). Zick and Homsy (1982) reported a theoretical solution for Stokes flow through lattice packings of uniform spheres, which can be considered as a benchmark for the DNS. Our numerical results suggest mesh-independent results can be achieved with $D_{\min}/d_{\mathrm{c}} \geq 120$ where d_{c} is the CFD cell size near the grain surface and $D_{\min}$ is the minimum grain diameter (1.04 mm), and the corresponding relative error on the fluid-grain interaction force is 2.7% (Wang et al. 2025). With $D_{\min}/d_{\mathrm{c}} = 120$, we further confirm its numerical convergence by comparing with the results

of the numerical model shown in Fig. 4(a) with other cell sizes $D_{\min}/d_c$ = 73, 212 and 438. As shown in Fig. 4(c) which presents the relative error of the permeability obtained with a given mesh and the finest mesh, the mesh-independent requirement has already been met with the selected d_c as the relative error is smaller than 10^{-4}. The adopted mesh scheme contained approximately 84 million cells in total with a maximum aspect ratio of 5.8 and with only 10 faces with a skewness larger than 4. The whole domain was split into 512 sub-domains and distributed on four nodes with 128 computation cores each, and the elapsed time for one case including meshing and solving was approximately 1.75 hours.

Comparison of PNM with DNS

We first solved the permeation of a Newtonian fluid (water) using both DNS and PNM on the same 142-grain packing shown in Fig. 4(a). Two key metrics, i.e., the intrinsic permeability K and the grain drag F_d which is the streamwise component of the fluid-grain interaction force, were considered in the DNS-PNM comparison. Similar to the DNS, a ratio $D_{\min}/d_v$ where d_v is the voxel resolution was defined. Considering a balance between the performance and the computation load, the optimum was achieved at $D_{\min}/d_v = 37.8$, beyond which the errors of K and F_d no longer decreased significantly, i.e., leading to convergence on both metrics, as shown in Fig. 5(a) and (b) where the error is defined as the ratio of the absolute difference between the PNM and the DNS divided by the result of the DNS.

Furthermore, with the selected resolution, the average error in F_d was around 10%. The observed errors result from the difference between the PNM and the DNS models, essentially at the boundaries. Specifically, first, near the inlet and outlet, two buffer layers were set in the DNS model, while in the PNM, the inlet and outlet were regarded as two virtual pore nodes, as shown in Fig. 4(b). Second, no special treatment for the surrounding boundaries is needed in the PNM which is different from the free-slip boundary condition used in the DNS model. Last but not least, in the PNM, pore bodies are simplified as nodes whose geometries are neglected in solving the matrix conductance.

As F_d strongly depends on the pressure field, see Eqs. 4 and 5, we then provide a quantitative

comparison of normalized pore pressure, i.e.,

$$\tilde{P} = \frac{P - P_{\text{out}}}{P_{\text{in}} - P_{\text{out}}}. \tag{7}$$

where P_{in} and P_{out} are the pressure values at (or near) the inlet and outlet, respectively, see Fig. 4(a) and (b). Although the pore pressure solved by the PNM had a good overall agreement with the DNS as shown in Fig. 5(c), it still has a 14% error on average, and therefore the error in F_{d} originates largely from the error in the pressure field.

Notably, investigating the pressure $F_{\text{d,p}}$ and the viscous $F_{\text{d,v}}$ components of F_{d}, respectively, as shown in Fig.5(d) and (e) where the force is scaled by the Stokes drag, suggests that the proposed algorithm can give reliable values of $F_{\text{d,p}}$ while underestimating $F_{\text{d,v}}$. However, in the relatively dense granular materials that are of interest in geomechanics, we find that the grain drag is dominated by the pressure difference rather than the viscous shear, and as shown in Fig. 5(f), the viscous component accounts for less than 20% for most grains. Therefore, the inaccuracy in the $F_{\text{d,v}}$ calculation method is considered acceptable to estimate the overall grain drag.

We then solved for polymer fluid flow using the same DNS model and the pore network with the selected resolution, as shown in Fig. 4 but with a power-law rheology, i.e., PHPA06 (see Table 2). Fig. 6(a) shows the comparison of Darcy velocity $|\mathbf{q}|$ vs. the pressure gradient $|\nabla P|$. The PNM captures the flow pattern, though the predicted values of $|\mathbf{q}|$ are slightly lower than the DNS due to the abovementioned model differences. More importantly, as shown in Fig. 6(b), with the selected resolution, the average error in the F_{d} values remains around 10% for the non-Newtonian fluid flow which is consistent with Newtonian flow. This suggests that the accuracy of F_{d} calculated from the PNM is almost independent of the rheological model.

RESULTS AND DISCUSSION

Via the PNM, we can achieve a simulation on a much larger sample with an acceptable computational load, and reach a reliable representative elementary volume (REV) analysis. For example, as shown in Fig. 4(d), the PSD of the 142-grain packing used in Section 3 has an

obvious deviation from the target (Ejezie A) one, while the 706-grain packing on which the PNM is conducted for the following accurately reproduces the target distribution.

Effects of non-Newtonian rheology

The polymer modeled here is based on the experiments of Lam et al. (2015) with a concentration of 0.6 kg/m^3; its rheological parameters are listed in Table 2.

Referring to Suo et al. (2025) it is important to appreciate three key features of polymer fluid flow in porous media:

1. Three flow regimes are identified as shown in Fig. 7(a), i.e., the Darcy regime (DR) at low $|\nabla P|$ in which $|\mathbf{q}| \propto |\nabla P|$, the power-law regime (PR) at high $|\nabla P|$ in which $|\mathbf{q}| \propto |\nabla P|^{1/n}$, and a transition regime (TR) bridges these two regimes, where the power index gradually changes from 1 to $1/n$.
2. At macro-scale, the flow can be described using a generalized Darcy's law,

$$\boldsymbol{q} = -\frac{K}{\mu_{\text{eff}}(|\nabla P|, r_{\text{eff}})}\nabla P, \tag{8}$$

   where μ_{eff} is the effective viscosity as a function of $|\nabla P|$ and the characteristic length of the porous medium r_{eff}. One can refer to Suo et al. (2025) for the explicit expressions of μ_{eff} and r_{eff}.
3. At the micro-scale, the shear-thinning rheology can enhance the flow heterogeneity and preferential pathways form through the larger, faster-flowing portions of the pore space in the PR.

In the subsequent analyses, we define normalized parameters with a tilde, by dividing by their values at the lowest $|\nabla P|$ simulated, i.e., 0.98 Pa/m. Fig. 7(b) shows the drag force of each complete grain. In the DR, the drag force is proportional to $|\nabla P|$, i.e., $\tilde{F}_{\text{d}}$ is a constant for all grains at a certain $|\tilde{\nabla P}|$. However, once $|\nabla P|$ increases so that the flow is in the transitional regime, while the average value of $\tilde{F}_{\text{d}}$ still increases linearly with $|\tilde{\nabla P}|$, the $\tilde{F}_{\text{d}}$ value for individual grains begins to

deviate from the average value. The extent of this variation in $\tilde{F}_\mathrm{d}$ can be quantified by considering the ratio of the standard deviation of $\tilde{F}_\mathrm{d}$ to the average $\tilde{F}_\mathrm{d}$ value, which we call the relative standard deviation Std($\tilde{F}_\mathrm{d}$)/Avg($\tilde{F}_\mathrm{d}$). As shown in Fig. 7(c), this variation attains a steady-state or constant value in the PR. We can further define a transition gradient $|\tilde{\nabla P}|_\mathrm{t}$ corresponding to the peak value of the slope of the relative standard deviation, beyond which the impact of these variations should be considered. As suggested in Fig. 7(a), the transition of $\tilde{F}_\mathrm{d}$ from having similar values for all grains, to displaying significant deviations occurs in the TR.

The transition in $\tilde{F}_\mathrm{d}$ results from the change in local conductance. Fig. 7(d) and (f) show the evolution of $\tilde{F}_\mathrm{d}$ for two characteristic grains with the maximum and the minimum $\tilde{F}_\mathrm{d}$ at the maximum $|\tilde{\nabla P}|$, respectively. The transition stages can be observed in the TR, after which $\tilde{F}_\mathrm{d}$ linearly increases with $|\tilde{\nabla P}|$ again in the PR. Polymer fluids have a shear-dependent viscosity and therefore the polymer conductance depends not only on the matrix geometry but also on the flow condition, especially in the TR. Specifically, larger pores have larger relative conductance due to the rather lower effective viscosity of the polymer, forming the so-called preferential pathways in the TR and resulting in the redistribution of pore pressures in the pore network, as shown in Fig. 7(e) and (g). For a given grain, the deviation of $\tilde{F}_\mathrm{d}$ from the average value is due to the unbalanced changes of pore pressures in its upstream and downstream neighboring pores. Notably, pressure redistribution ceases at the end of the TR and therefore $\tilde{F}_\mathrm{d}$ increases linearly with pressure gradient afterwards.

We investigated the distribution of the drag force as a function of grain size and spatial position. Fig. 8(a) indicates that the drag force on smaller grains varies more significantly. In this packing, the drag force of small grains varies by a factor of two around the average. Larger grains see less fluctuation in the drag force about the average. As shown in Fig. 8(b), no clear correlation between the grain drag and its spatial position was observed in a random packing.

Effects of polymer concentration

The rheological properties of a polymer fluid depend on its concentration. According to rheometer tests (Lam et al. 2015), as the concentration increases, the upper (μ_0) and lower (μ_∞)

bounds of viscosity increase, while zero shear rate ($\dot{\gamma}_0$) and power-law index (n) fall slightly. The polymer considered here covers a wide range of concentration from 0.4 to 1.0 kg/m^3, whose rheological parameters are identified by fitting the rheometer data (Lam et al. 2015), as listed in Table 2.

We simulated flow in the virtual sphere packing, Ejezie A, (see Table 1), with varying polymer concentrations. Fig. 9(a) shows the comparison on the grain drag $\tilde{F}_\mathrm{d}$. The average values for all cases with various concentrations are collapsed on one line; however, the transition from average to variable behavior changes with polymer concentration. As observed in Fig. 9(b), the transition gradient $|\tilde{\nabla P}|_\mathrm{t}$ increases with concentration. According to our theoretical analysis on polymer fluid flow in porous media (Suo et al. 2025), the transition gradient between the DR and the TR is proportional to $\mu_0\dot{\gamma}_0/\sqrt{K}$. Since the drag force pattern transition results from the flow regime transition as analyzed above, this conclusion can be extended to $|\tilde{\nabla P}|_\mathrm{t}$, i.e., $|\tilde{\nabla P}|_\mathrm{t} \propto \mu_0\dot{\gamma}_0/\sqrt{K}$, which is verified in Fig. 3(c).

Effects of sand type

Another factor impacting the distribution of $\tilde{F}_\mathrm{d}$ is the sand type, which is characterized by its PSD and porosity. We will use the VSPs described in Suo and Wang (2024). The key geometric parameters ϕ, D_{50} and K of all VSPs are summarized in Table 1.

To evaluate $|\nabla P|_\mathrm{t}$, we ran the PNM on all nine VSPs considered in this study with four polymer concentrations; the predicted $|\tilde{\nabla P}|_\mathrm{t}$ values are shown in Table 3. As shown in Fig. 10, we find the following empirical relationship for $|\nabla P|_\mathrm{t}$

$$|\nabla P|_\mathrm{t} \approx 0.459\mu_0\dot{\gamma}_0/\sqrt{K}. \tag{9}$$

Engineering significance

EFFC/DFI (2019) has provided a general explanation of the principles of excavation support fluids including bentonite and polymer. With the focus on polymer fluids, we adapted the schematic of an excavation for a diaphragm wall (Fig. 4) in EFFC/DFI (2019), as shown in Fig. 11(a) where

the polymer support fluid (in orange) permeates the surrounding sands through the excavation surface to displace the ground water (in blue). The difference in density of water and polymer solution is less than 0.2% and so both fluids are assumed to have the same density. The interface between the two fluids is assumed to be vertically oriented and sharp, since the polymer viscosity is much larger than water which is being displaced. Based on these two assumptions, the problem can be simplified as a one-dimensional model as shown in Fig. 11(b). In the polymer-saturated phase, the flow can be described using the generalized Darcy's law, i.e., Eq. 8 while Darcy's law is used in the water-saturated phase. At the interface ($x = x_\mathrm{p}$), we have

$$P(x = x_\mathrm{p}^+) = P(x = x_\mathrm{p}^-), \tag{10}$$

according to the pressure continuity; and

$$q(x = x_\mathrm{p}^+) = q(x = x_\mathrm{p}^-) \tag{11}$$

from conservation of mass. At the left and right boundaries, the pressure values are fixed as $\rho_\mathrm{w} g y_0$ at $x = 0$ and 0 at $x = x_\mathrm{w}$, where y_0 is the head difference between the polymer and water phases. We finally obtain a non-linear equation regarding the pressure gradient in the polymer-saturated phase $|\nabla P|$,

$$|\nabla P| = \frac{\rho_\mathrm{w} g y_0}{x_\mathrm{w}} \frac{\mu_\mathrm{eff}}{\mu_\mathrm{w}(x_\mathrm{w} - x_\mathrm{p}) + \mu_\mathrm{eff} x_\mathrm{p}}. \tag{12}$$

As an exemplar we took the sand Ejezie A (see Table 1) supported by PHPA12 (see Table 2) with $y_0 = 2$ m. The dynamics of polymer permeation depend on the horizontal length of the domain, i.e., x_w. As suggested by the evolution of x_p in Fig. 11(c), a larger x_w leads to a slower permeation of polymer as the total flow resistance and especially the pressure drop within the water phase increases with x_w. As a consequence, $|\nabla P|$ significantly decreases with increasing x_w at the very beginning of permeation as shown in Fig. 11(d). By additionally assuming $P(x = x_\mathrm{p}^+) = P(x = x_\mathrm{p}^-) = 0$, i.e., the flow resistance of the water phase is ignored since no pressure drop occurs within the water

phase, an upper-limit estimation of x_p is developed. The polymer viscosity is much larger than water; even the lower bound, μ_∞ is around 10 times larger than μ_w. Therefore, the pressure drop within the water is generally much lower than that in the polymer phase. Thus this idealized case gives comparable results to the case with $x_w = 100$ m as shown in 11(c) and (d). The upper limit obtained by neglecting the head loss in the water phase could be a reasonable estimation of the polymer loss in engineering practice if the exact x_w is not accessible.

From the continuum-scale modeling, we can estimate the total support force in the polymer phase as $F = |\nabla P| x_p$, shown in Fig. 11(e), which can be potentially used in trench stability analysis following the limit equilibrium method (Filz et al. 2004).

The total support force on sands originates from the drag on each sand grain at the microscopic scale, as conceptualized in Fig. 11(f). As analyzed above, when $|\nabla P| > |\nabla P|_t$, $\tilde{F}_d$ is different for different grains suggesting some grains have a larger drag force which is beneficial to excavation support, while the drag on others is lower than the expected value which may risk the stability of the excavation. To quantify the variation of grain drag, a specific cumulative distribution function of $F_d/\bar{F}_d$ in the PR is introduced as shown in Fig. 11(g). By setting a confidence level of 95%, i.e., 95% grains have sufficient drag, we can determine a reduction factor, as marked in Fig. 11(g), which characterizes the deviation between grain-scale and continuum-scale modeling. Therefore, to guarantee excavation design, one should consider modifying F by the reduction factor if $|\nabla P| > |\nabla P|_t$. Fig. 10(b) shows the reduction factors for all sand samples with various polymer fluids; they slightly decrease with the polymer concentration, but their values are around 0.8 on average and larger than 0.75 for all cases.

CONCLUSIONS

In this study, we employed pore-network modeling to numerically investigate the grain drag forces induced by polymer fluid flow in sands. The findings provide valuable insights into the grain-scale effects of polymer flow and their implications for the use of polymer fluids in excavation support. The key conclusions of this work are as follows:

1. As the shear-thinning rheology enhances the heterogeneity in the flow field, we found the grain drag does not scale linearly with pressure gradient, $|\nabla P|$, once $|\nabla P|$ excces a critical threshold value, $|\tilde{\nabla P}|_{\mathrm{t}}$.
2. The critical pressure gradient $|\nabla P|_{\mathrm{t}}$ shows a dependency on the fluid rheology (μ_0 and $\dot{\gamma}_0$) and the intrinsic permeability (K). Specifically it is proportional to $\mu_0\dot{\gamma}_0/\sqrt{K}$ where the proportionality coefficient was determined to be 0.459 through fitting to simulations on nine sand packs with four polymer concentrations each.
3. A one-dimensional continuum model was developed based on the generalized Darcy's law to simulate polymer fluid permeation adjacent to an open excavation. This model provides estimates of the pressure gradient and total support force at the macro scale. There is a potential to use this model in the excavation stability analysis, for example by implementation in a coupled finite element formulation.
4. To secure a safe design of excavation support, we recommend correcting the macroscopic support force by multiplying a reduction factor if the applied pressure gradient exceeds $|\nabla P|_{\mathrm{t}}$. This reduction accounts for the flow heterogeneity in the fluid-particle interaction forces acting on individual grains that arises due to the heterogeneous flow field.

DATA AVAILABILITY STATEMENT

The code used in this study can be found in https://github.com/ImperialCollegeLondon/Pore-Network-Modeling-of-Polymer-Flows.

ACKNOWLEDGEMENTS

This work was funded by the EPSRC grant EP/X034305/1: Permeation of polymer fluids in soils (PoPFS) and the UKRI Access to HPC call APP36940 (ARCHER2): Modelling permeation of polymer support fluids in soils using a combined CFD and DEM approach.

REFERENCES

Blunt, M. J. (2017). *Multiphase flow in permeable media: A pore-scale perspective*. Cambridge University Press.

Blunt, M. J., Bijeljic, B., Dong, H., Gharbi, O., Iglauer, S., Mostaghimi, P., Paluszny, A., and Pentland, C. (2013). "Pore-scale imaging and modelling." *Advances in Water resources*, 51, 197–216.

Bryant, S. and Blunt, M. (1992). "Prediction of relative permeability in simple porous media." *Physical review A*, 46(4), 2004.

Carey, T. J., Stone, N., and Kutter, B. L. (2020). "Grain size analysis and maximum and minimum dry density testing of ottawa f-65 sand for leap-ucd-2017." *Model tests and numerical simulations of liquefaction and lateral spreading: LEAP-UCD-2017*, Springer, 31–44.

Chareyre, B., Cortis, A., Catalano, E., and Barthélemy, E. (2012). "Pore-scale modeling of viscous flow and induced forces in dense sphere packings." *Transport in Porous Media*, 94, 595–615.

Climent, N., Arroyo, M., O'Sullivan, C., and Gens, A. (2014). "Sand production simulation coupling DEM with CFD." *European Journal of Environmental and Civil Engineering*, 18(9), 983–1008.

Dong, H. and Blunt, M. J. (2009). "Pore-network extraction from micro-computerized-tomography images." *Physical Review E—Statistical, Nonlinear, and Soft Matter Physics*, 80(3), 036307.

EFFC/DFI (2019). *Guide to Support Fluids for Deep Foundations*. European Federation of Foundation Contractors / Deep Foundations Institute.

Ejezie, J. O., Jefferis, S. A., Lam, C., Sedighi, M., and Ahmad, S. M. (2021). "Permeation behaviour of PHPA polymer fluids in sand." *Géotechnique*, 71(7), 561–570.

Filz, G. M., Adams, T., and Davidson, R. R. (2004). "Stability of long trenches in sand supported by bentonite-water slurry." *Journal of geotechnical and geoenvironmental engineering*, 130(9), 915–921.

Jefferis, S. A. and Lam, C. (2013). "Polymer support fluids: use and misuse of innovative fluids in geotechnical works." *Proceedings of the 18 th International Conference on Soil Mechanics and*

Geotechnical Engineering, Paris.

Kumar, S., Yadav, B. D., and Raj, R. (2024). "A review on the application of biopolymers (xanthan, agar and guar) for sustainable improvement of soil." *Discover Applied Sciences*, 6(8), 393.

Lam, C. and Jefferis, S. A. (2014). "The use of polymer solutions for deep excavations: lessons from far eastern experience." *HKIE Transactions*, 21(4), 262–271.

Lam, C. and Jefferis, S. A. (2018). *Polymer support fluids in civil engineering*. Institution of Civil Engineers Publishing London.

Lam, C., Martin, P. J., and Jefferis, S. A. (2015). "Rheological properties of PHPA polymer support fluids." *Journal of Materials in Civil Engineering*, 27(11), 04015021.

Liu, Y., Yin, Z.-Y., Wang, L., and Hong, Y. (2021). "A coupled CFD–DEM investigation of internal erosion considering suspension flow." *Canadian Geotechnical Journal*, 58(9), 1411–1425.

Mačak, J., Fintzi, N., Gamet, L., Pierson, J.-L., and Morin, M. (2025). "Particle-resolved simulations of flows through sphere, cylinder or spherocylinder assemblies: automatic workflow." *OpenFOAM journal*.

Morimoto, T., O'Sullivan, C., and Taborda, D. M. G. (2024). "Applying network modeling to determine seepage-induced forces on soil particles." *Journal of Geotechnical and Geoenvironmental Engineering*, 150(5), 04024029.

Patankar, S. V. and Spalding, D. B. (1983). "A calculation procedure for heat, mass and momentum transfer in three-dimensional parabolic flows." *Numerical prediction of flow, heat transfer, turbulence and combustion*, Elsevier, 54–73.

Qu, M.-L., Blunt, M. J., Fan, X., Foroughi, S., Yu, Z.-T., and Lin, Q. (2023). "Pore-to-mesoscale network modeling of heat transfer and fluid flow in packed beds with application to process design." *AIChE Journal*, 69(12), e18213.

Qu, M.-L., Yang, J., Foroughi, S., Zhang, Y., Yu, Z.-T., Blunt, M. J., and Lin, Q. (2024). "Pore-to-meter scale modeling of heat and mass transport applied to thermal energy storage: How local thermal and velocity fluctuations affect average thermal dispersivity." *Energy*, 296, 131147.

Raeini, A. Q., Bijeljic, B., and Blunt, M. J. (2017). "Generalized network modeling: Network

extraction as a coarse-scale discretization of the void space of porous media." *Physical Review E*, 96(1), 013312.

Rodríguez de Castro, A., Agnaou, M., and Gostick, J. (2023). "Predicting shear-thinning fluid flows in porous media using pore network modeling: Simulations and experimental validation." *Transport in Porous Media*, 149(2), 453–478.

Salomon, J., Morimoto, T., Patino-Ramirez, F., and O'Sullivan, C. (2024). "Quantifying shear-induced permeability changes in medium-loose sands." *Journal of Geotechnical and Geoenvironmental Engineering*, 150(2), 04023133.

Sanvitale, N., Zhao, B., Bowman, E., and O'Sullivan, C. (2023). "Particle-scale observation of seepage flow in granular soils using PIV and CFD." *Géotechnique*, 73(1), 71–88.

Sorbie, K. (1991). *Polymer-improved oil recovery*. Springer Science & Business Media.

Suo, S., Foroughi, S., Blunt, M. J., and O'Sullivan, C. (2025). "Pore-network modeling of polymer flow in porous media." *Computers and Geotechnics*, 182, 107142.

Suo, S. and Wang, Y. (2024). "Virtual sand packing, <https://github.com/SeeSawGo/VirtualSandPacking/>.

Suo, S., Zhai, C., Kamlah, M., and Gan, Y. (2023). "An unexplored regime of binary packing under extreme mixture conditions." *Powder Technology*, 428, 118802.

Taylor, H., O'sullivan, C., and Sim, W. (2016). "Geometric and hydraulic void constrictions in granular media." *Journal of Geotechnical and Geoenvironmental Engineering*, 142(11), 04016057.

Taylor, H. F., O'Sullivan, C., Sim, W. W., and Carr, S. J. (2017). "Sub-particle-scale investigation of seepage in sands." *Soils and Foundations*, 57(3), 439–452.

Valvatne, P. H. and Blunt, M. J. (2004). "Predictive pore-scale modeling of two-phase flow in mixed wet media." *Water resources research*, 40(7).

Wang, Y., Suo, S., Bortolotto, M. S., O'Sullivan, C., and Blunt, M. J. (2025). "Particle-scale simulation of polymer fluid permeation in sand." *International Journal of Geomechanics*, 25(11), 06025016.

Yang, J. and Sze, H. (2011). "Cyclic behaviour and resistance of saturated sand under non-

symmetrical loading conditions." *Géotechnique*, 61(1), 59–73.

Zick, A. and Homsy, G. (1982). "Stokes flow through periodic arrays of spheres." *Journal of fluid mechanics*, 115, 13–26.

List of Tables

1 Key geometry parameters of virtual sand packings. 21

2 Parameters of the polymer fluids obtained by fitting rheometer test data, see Fig. 1 for notations. 22

3 Transition gradient $|\tilde{\nabla P}|_t$ [kPa/m] of all VSPs with PHPA polymer concentrations ranging from 0.4 kg/m^3 (PHPA04) to 1.0 kg/m^3 (PHPA10). 23

Tag	Porosity ϕ	Intrinsic permeability K [m^2]	Particle size D_{50} [mm]
Ejezie A (LBS)	0.345	2.98×10^{-9}	2.55
Ejezie B (LBS)	0.355	1.02×10^{-9}	2.37
Ejezie C (LBS)	0.351	2.84×10^{-10}	0.74
Taylor Cu1.5 (LBS)	0.415	4.42×10^{-10}	0.65
Taylor Cu2.0 (LBS)	0.390	5.83×10^{-10}	0.90
Taylor Cu3.0 (LBS)	0.386	4.69×10^{-10}	0.95
Taylor Cu4.0 (LBS)	0.394	2.08×10^{-10}	0.73
Toyoura (TS)	0.350	2.39×10^{-11}	0.20
Ottawa (OS)	0.350	2.11×10^{-11}	0.20

TABLE 1. Key geometry parameters of virtual sand packings.

Tag	Concentration [kg/m^3]	μ_0 [Pa·s]	$\dot{\gamma}_0$ [1/s]	μ_∞ [Pa·s]	n
PHPA02	0.2	1.11	0.00563	0.00389	0.467
PHPA04	0.4	8.77	0.00242	0.00698	0.376
PHPA06	0.6	16.52	0.00308	0.00871	0.324
PHPA08	0.8	40.96	0.00186	0.0115	0.302
PHPA10	1.0	64.73	0.00228	0.0136	0.262
PHPA12	1.2	100.72	0.00234	0.0188	0.256

TABLE 2. Parameters of the polymer fluids obtained by fitting rheometer test data, see Fig. 1 for notations.

Soil tag \ Concentration (kg/m^3)	0.4	0.6	0.8	1.0
Ejezie A (LBS)	0.207	0.460	0.595	1.11
Ejezie B (LBS)	0.340	0.685	1.09	2.12
Ejezie C (LBS)	0.510	1.26	1.87	3.58
Taylor Cu1.5 (LBS)	0.511	1.26	1.80	3.52
Taylor Cu2.0 (LBS)	0.503	1.41	2.04	3.89
Taylor Cu3.0 (LBS)	0.517	1.28	1.90	3.72
Taylor Cu4.0 (LBS)	0.753	1.81	2.71	5.17
Toyoura (TS)	2.09	4.86	7.28	13.9
Ottawa (OS)	2.17	5.06	7.47	14.3

TABLE 3. Transition gradient $|\tilde{\nabla P}|_{\mathrm{t}}$ [kPa/m] of all VSPs with PHPA polymer concentrations ranging from 0.4 kg/m^3 (PHPA04) to 1.0 kg/m^3 (PHPA10).

List of Figures

1 The truncated power law model for characterizing the rheology of polymer fluids. . 26

2 Network extraction workflow: (a) The virtual sand packing, and (b) its corresponding binary image (b) and marked image (c). (d) The extracted pore network and (e) a zoomed-in schematic of the grain-pore interface. 27

3 Calculation schematics of (a) the form drag and (b) the skin friction. 28

4 (a) Computation domain of the benchmark DNS and (b) the corresponding pore-network model. (c) Relative error of permeability solved in DNS vs. $D_{\min}/d_{\mathrm{c}}$. (d) Particle size distribution of the grains when the packing porosity is 0.343. 29

5 Newtonian fluid (water) flow in the benchmark model. Relative error in the calculation of intrinsic permeability (a) and the grain drag (b) calculated from the PNM relative to the DNS benchmark with varying ratios of the minimum grain diameter $D_{\min}$ on the voxel resolution d_{v}. The shaded area indicates the variability range of the relative error. Using the mesh resolution indicated by the pentagram, comparisons of the normalized pore pressure (c), the pressure (d) and viscous (e) components of the grain drag between the PNM and the DNS. (f) histogram of the proportion of the viscous force contribution to the overall fluid particle interaction force in the DNS benchmark. 30

6 Polymer fluid (PHPA06) flow in the benchmark model. (a) Darcy velocity $|\mathbf{q}|$ as a function of the pressure gradient $|\nabla P|$. (b) Relative error in the calculation of the grain drag from the PNM relative to the DNS benchmark with varying pressure gradient. The shaded area indicates the variability range of this error. 31

7 For the sand packing (Ejezie A), (a) normalized Darcy velocity $|\tilde{\mathbf{q}}|$, (b) drag force $\tilde{F}_\mathrm{d}$ of all complete grains and (c) its standard deviation of $\tilde{F}_\mathrm{d}$ as a function of the normalized pressure gradient $|\tilde{\nabla P}|$. Three flow regimes, namely the Darcy regime, transition regime and power-law regime are identified in (a) and a transition gradient is marked by dotted lines, at which the slope of the relative deviation reaches the peak. The evolution of $\tilde{F}_\mathrm{d}$ and the neighboring pore pressures $\tilde{P}$ of grains with the maximum (d, e) and the minimum (f, g) $\tilde{F}_\mathrm{d}$ at the maximum $|\tilde{\nabla P}|$. 32

8 The distribution of grain drag $F_\mathrm{d}/\bar{F}_\mathrm{d}$ in the power-law regime with (a) grain diameter $D/\bar{D}$ and (b) spatial position for each complete grain. The color bar in (b) indicate the value of $F_\mathrm{d}/\bar{F}_\mathrm{d}$. The parameter with bar here means the average value. 33

9 Sand packing (Ejezie A) with polymer concentrations of 0.4, 0.6, 0.8 and 1.0 kg/m^3. (a) Variation in normalized drag force $\tilde{F}_\mathrm{d}$ of all complete grains with normalized pressure gradient $|\tilde{\nabla P}|$ and (b) the corresponding relative standard deviation of $\tilde{F}_\mathrm{d}$. On the right of (a) is a zoomed-in plot near the transition gradients. The transition gradient values are marked by dotted lines in (b). (c) Relationship between the normalized transition gradient $|\tilde{\nabla P}|_\mathrm{t}$ and $\mu_0\dot{\gamma}_0/\sqrt{K}$ (Fluid rheology parameters defined in Fig. 1, K is intrinsic permeability). 34

10 (a) Transition gradient $|\nabla P|_\mathrm{t}$ vs. $\mu_0\dot{\gamma}_0/\sqrt{K}$ and (b) reduction factor vs. polymer concentration for all virtual sand samples. 35

11 (a) Schematic of an excavation with polymer permeating the surrounding soil where $y0$ is the head difference between water and polymer phases. (b) 1D continuum-scale model. Dynamics of (c) the polymer front, (d) the pressure gradient and (e) the total support force in the polymer phase for sand Ejezie A (LBS) with PHPA12 at different boundary conditions. (f) Zoomed-in schematic of grains with flow-induced drag forces. (g) Passing percentage of grains with larger $\tilde{F}_\mathrm{d}$. 36

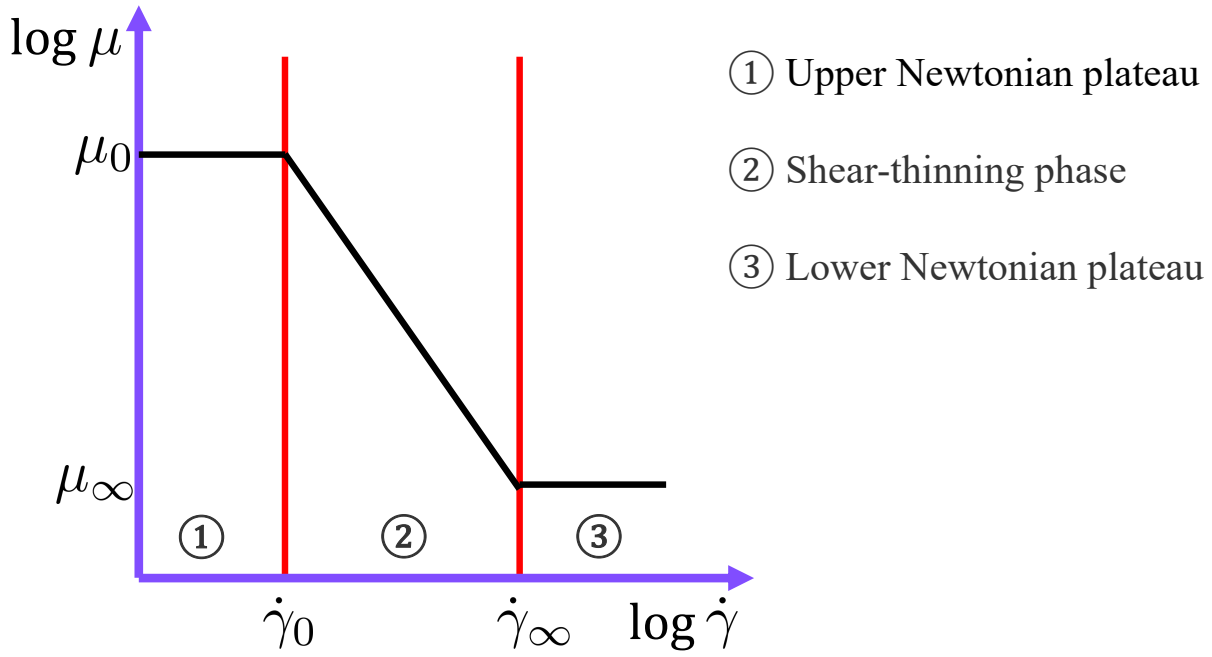


Fig. 1. The truncated power law model for characterizing the rheology of polymer fluids.

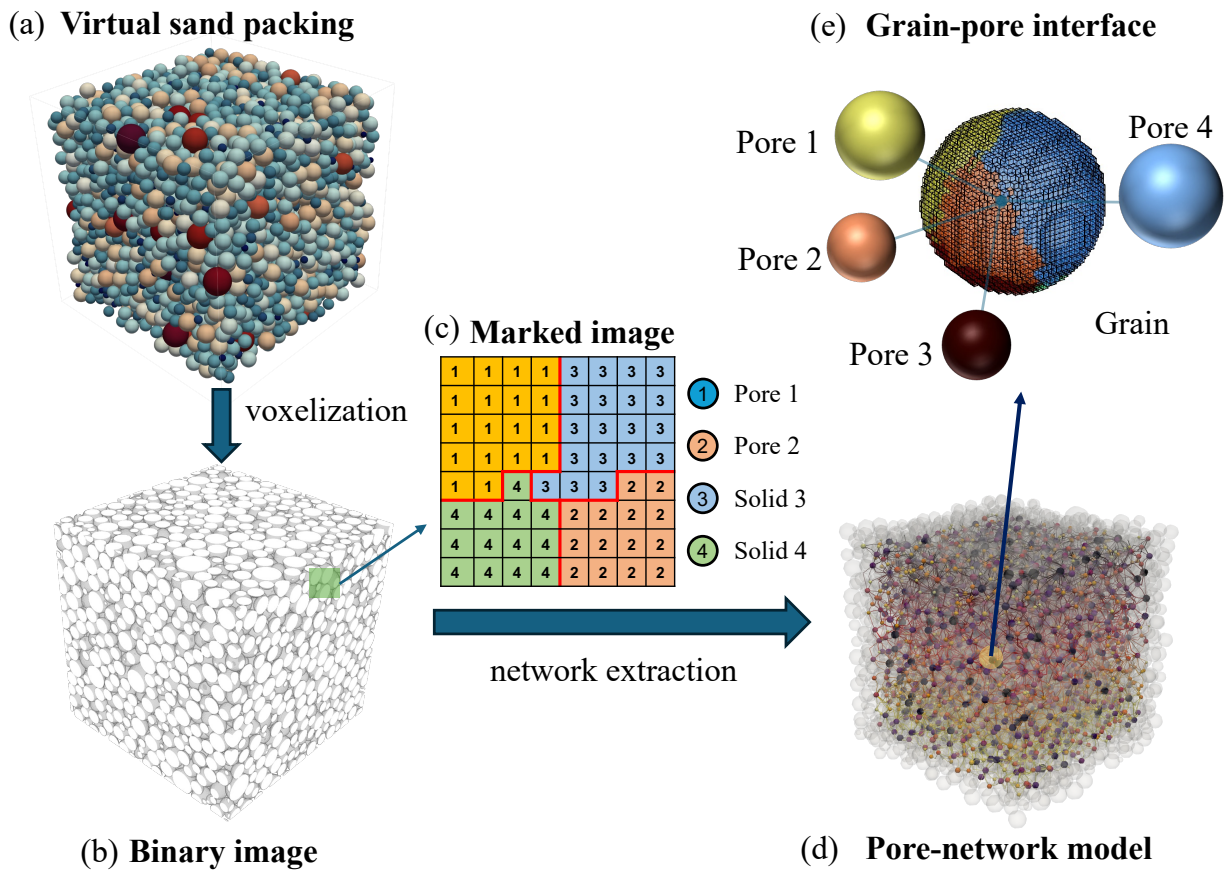


Fig. 2. Network extraction workflow: (a) The virtual sand packing, and (b) its corresponding binary image (b) and marked image (c). (d) The extracted pore network and (e) a zoomed-in schematic of the grain-pore interface.

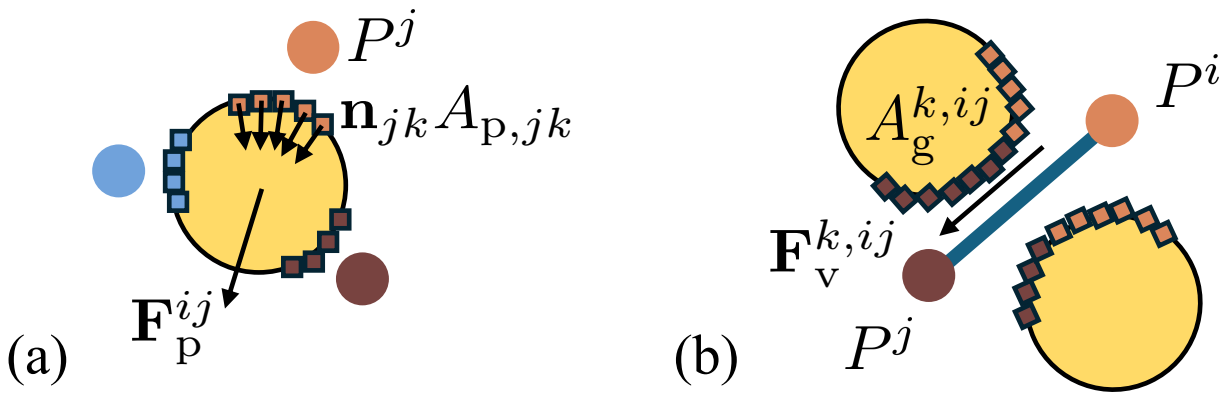


Fig. 3. Calculation schematics of (a) the form drag and (b) the skin friction.

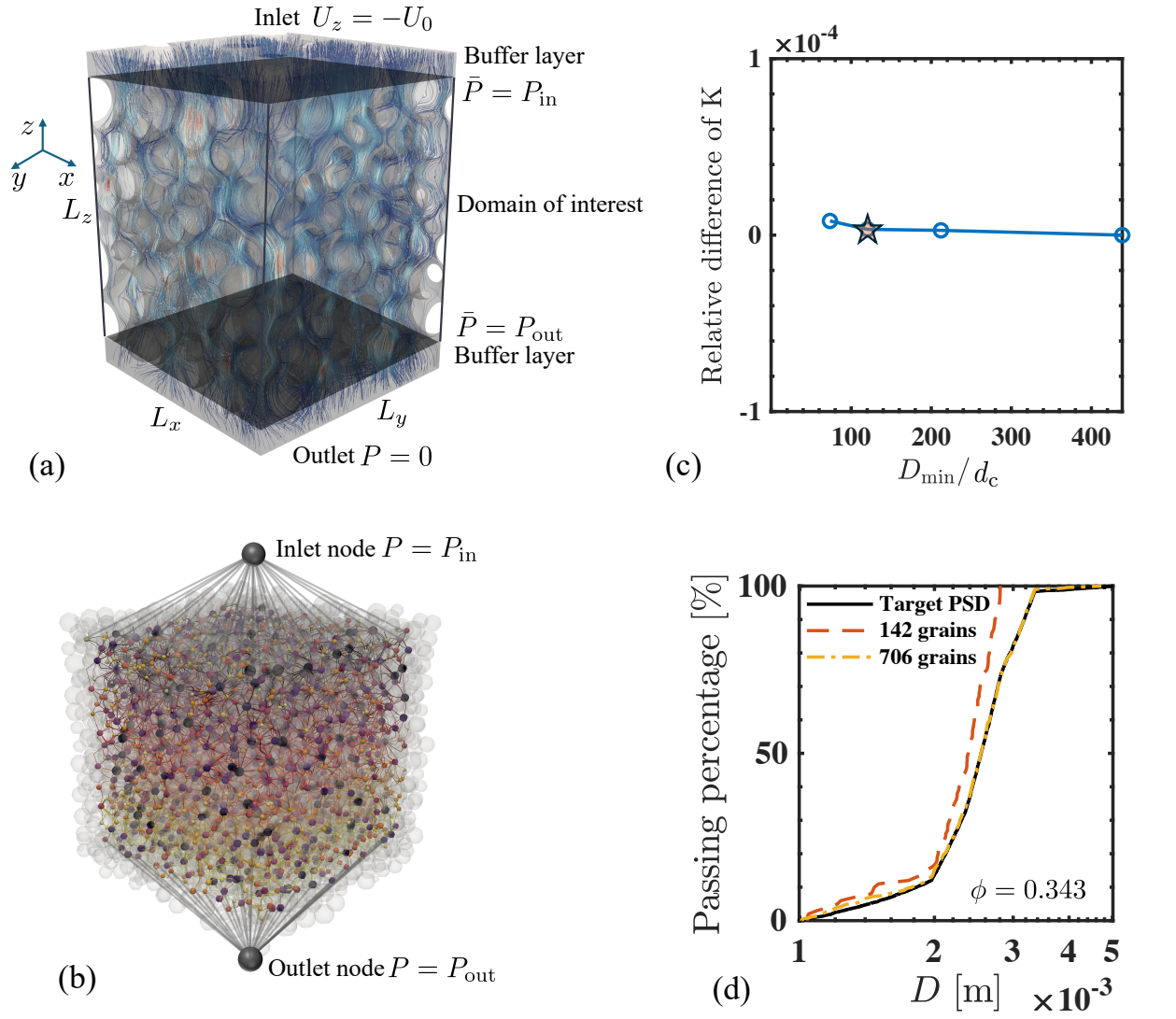


Fig. 4. (a) Computation domain of the benchmark DNS and (b) the corresponding pore-network model. (c) Relative error of permeability solved in DNS vs. $D_{\text{min}}/d_{\text{c}}$. (d) Particle size distribution of the grains when the packing porosity is 0.343.

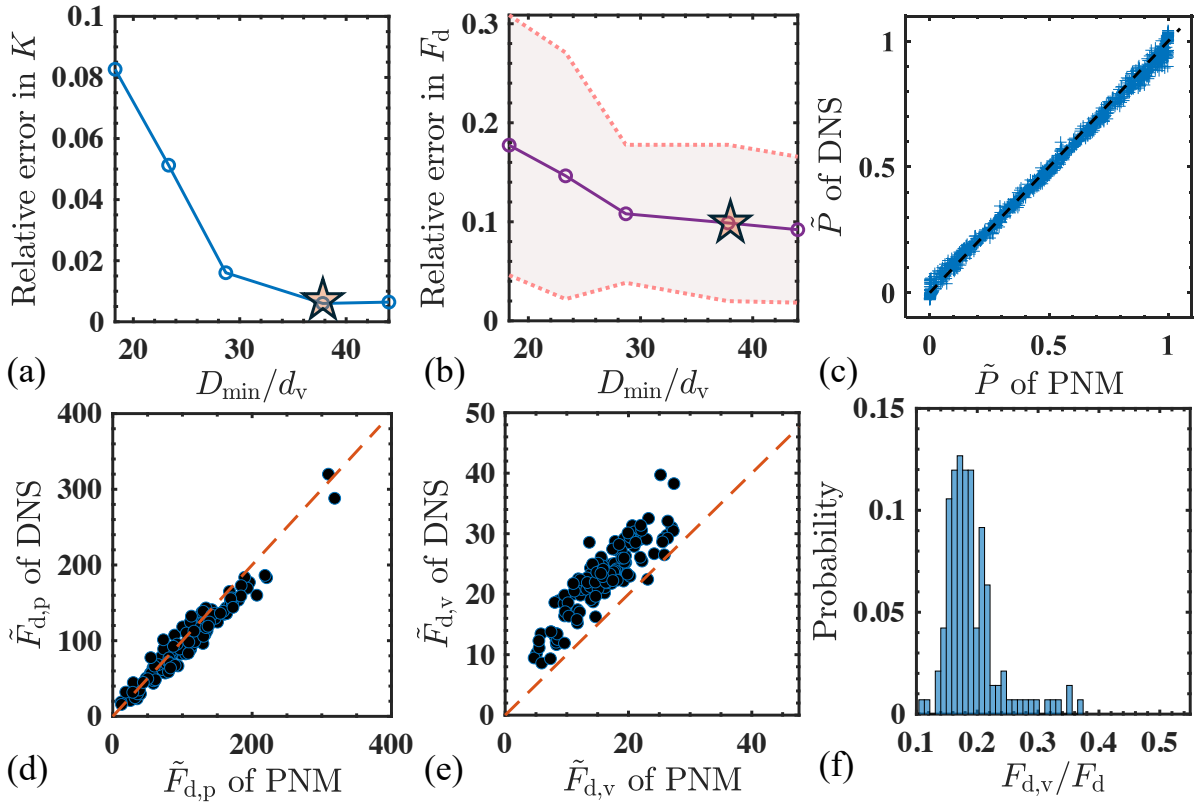


Fig. 5. Newtonian fluid (water) flow in the benchmark model. Relative error in the calculation of intrinsic permeability (a) and the grain drag (b) calculated from the PNM relative to the DNS benchmark with varying ratios of the minimum grain diameter $D_{\min}$ on the voxel resolution d_{v}. The shaded area indicates the variability range of the relative error. Using the mesh resolution indicated by the pentagram, comparisons of the normalized pore pressure (c), the pressure (d) and viscous (e) components of the grain drag between the PNM and the DNS. (f) histogram of the proportion of the viscous force contribution to the overall fluid particle interaction force in the DNS benchmark.

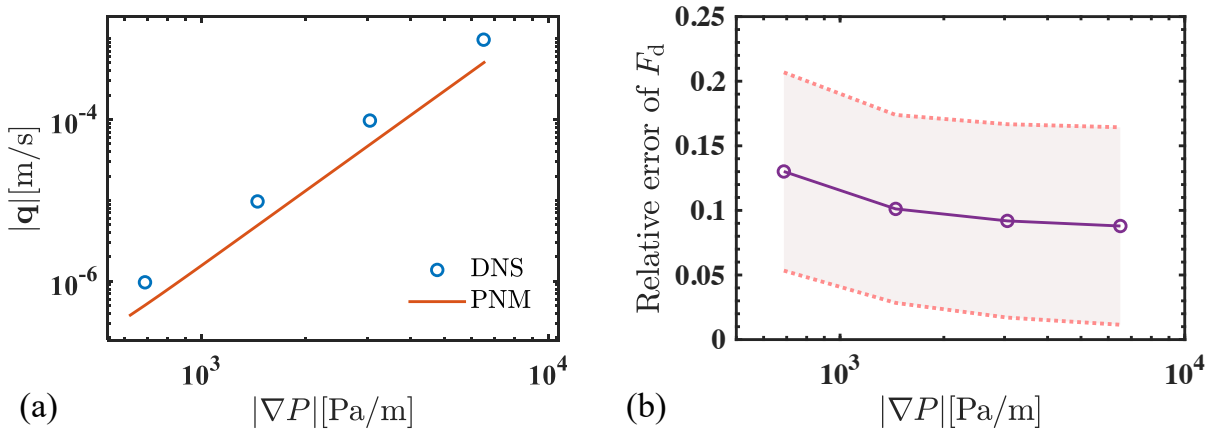


Fig. 6. Polymer fluid (PHPA06) flow in the benchmark model. (a) Darcy velocity $|\mathbf{q}|$ as a function of the pressure gradient $|\nabla P|$. (b) Relative error in the calculation of the grain drag from the PNM relative to the DNS benchmark with varying pressure gradient. The shaded area indicates the variability range of this error.

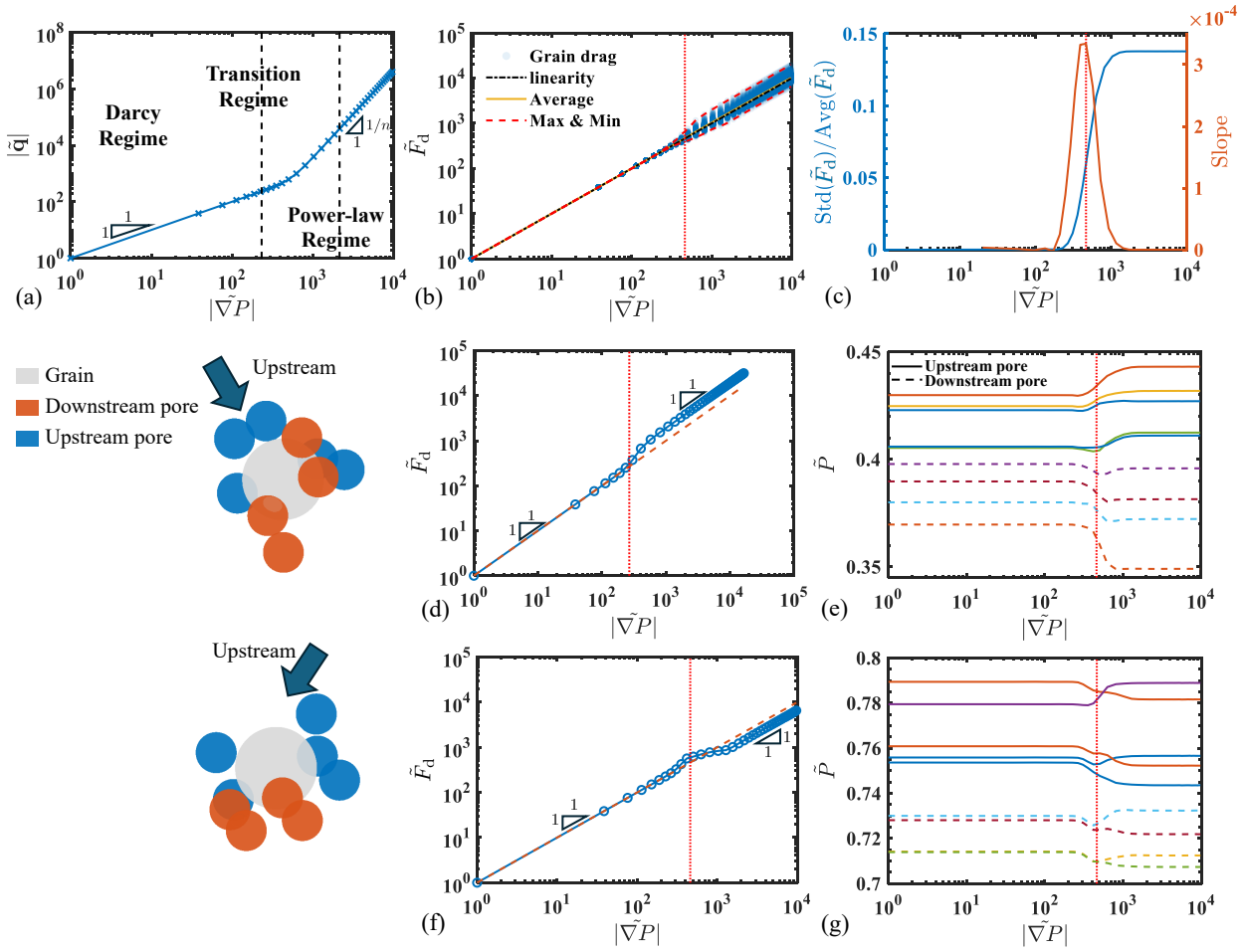


Fig. 7. For the sand packing (Ejezie A), (a) normalized Darcy velocity $|\tilde{\mathbf{q}}|$, (b) drag force $\tilde{F}_d$ of all complete grains and (c) its standard deviation of $\tilde{F}_d$ as a function of the normalized pressure gradient $|\tilde{\nabla}P|$. Three flow regimes, namely the Darcy regime, transition regime and power-law regime are identified in (a) and a transition gradient is marked by dotted lines, at which the slope of the relative deviation reaches the peak. The evolution of $\tilde{F}_d$ and the neighboring pore pressures $\tilde{P}$ of grains with the maximum (d, e) and the minimum (f, g) $\tilde{F}_d$ at the maximum $|\tilde{\nabla}P|$.

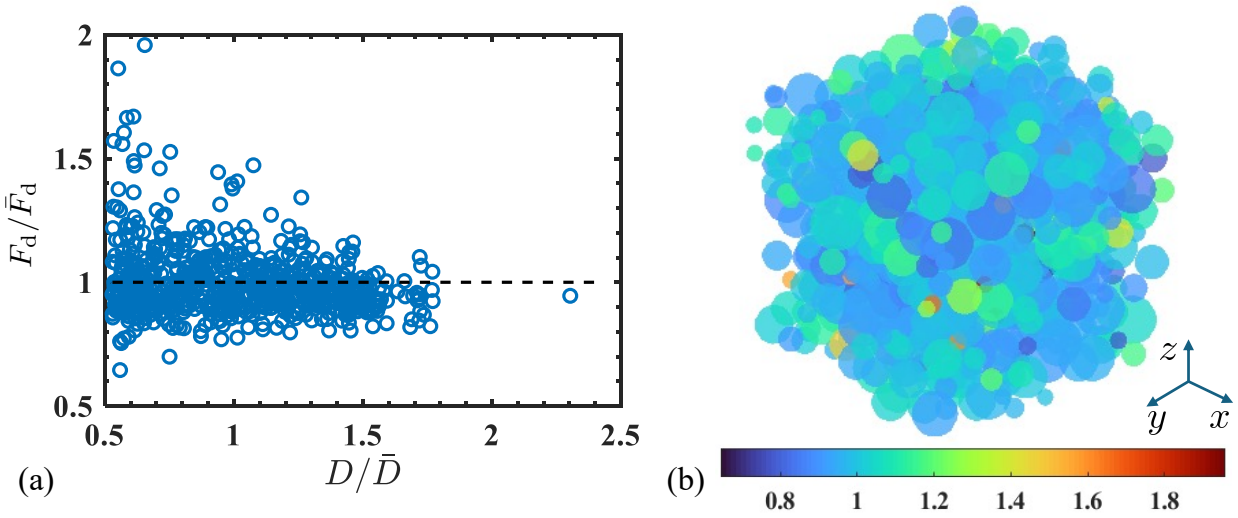


Fig. 8. The distribution of grain drag $F_d/\bar{F}_d$ in the power-law regime with (a) grain diameter $D/\bar{D}$ and (b) spatial position for each complete grain. The color bar in (b) indicate the value of $F_d/\bar{F}_d$. The parameter with bar here means the average value.

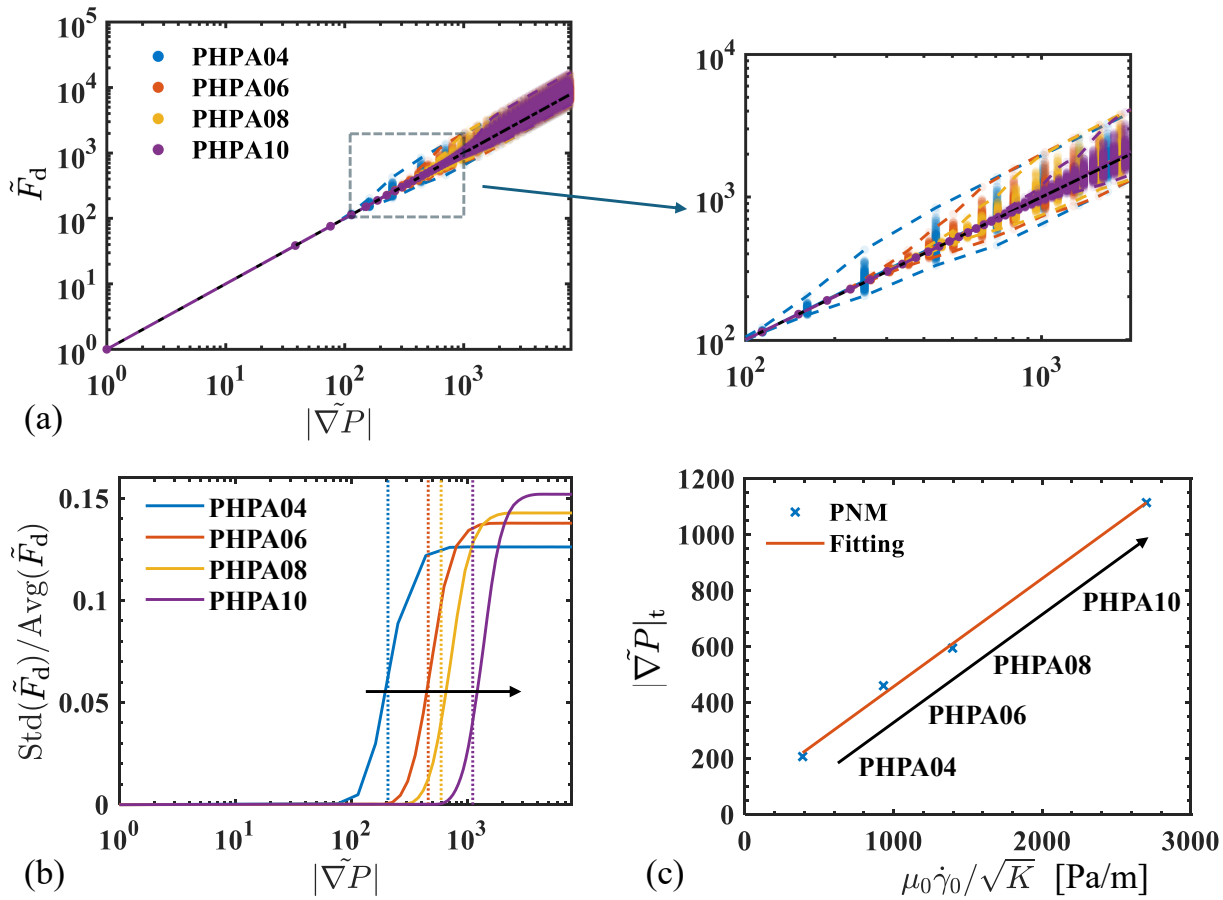


Fig. 9. Sand packing (Ejezie A) with polymer concentrations of 0.4, 0.6, 0.8 and 1.0 kg/m^3. (a) Variation in normalized drag force $\tilde{F}_\mathrm{d}$ of all complete grains with normalized pressure gradient $|\tilde{\nabla}P|$ and (b) the corresponding relative standard deviation of $\tilde{F}_\mathrm{d}$. On the right of (a) is a zoomed-in plot near the transition gradients. The transition gradient values are marked by dotted lines in (b). (c) Relationship between the normalized transition gradient $|\tilde{\nabla}P|_\mathrm{t}$ and $\mu_0\dot{\gamma}_0/\sqrt{K}$ (Fluid rheology parameters defined in Fig. 1, K is intrinsic permeability).

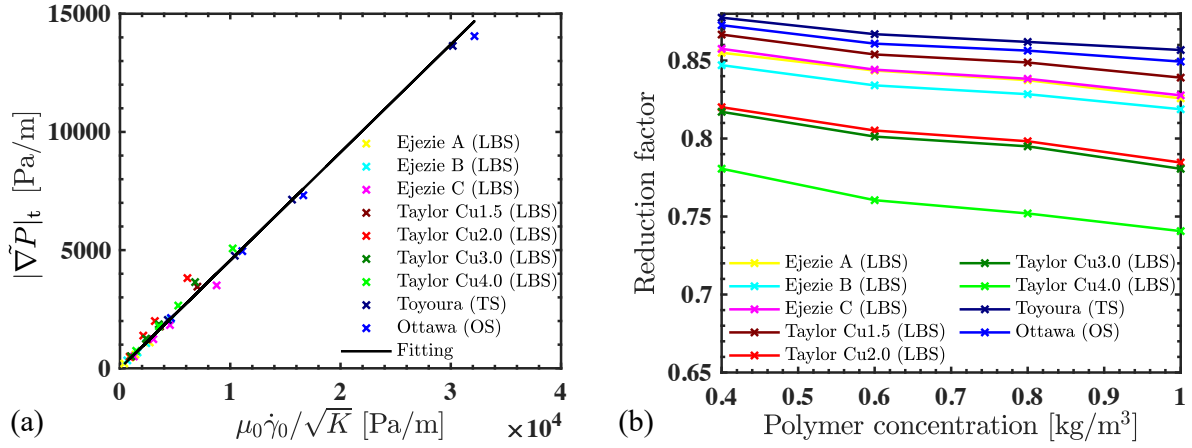


Fig. 10. (a) Transition gradient $|\nabla P|_t$ vs. $\mu_0\dot{\gamma}_0/\sqrt{K}$ and (b) reduction factor vs. polymer concentration for all virtual sand samples.

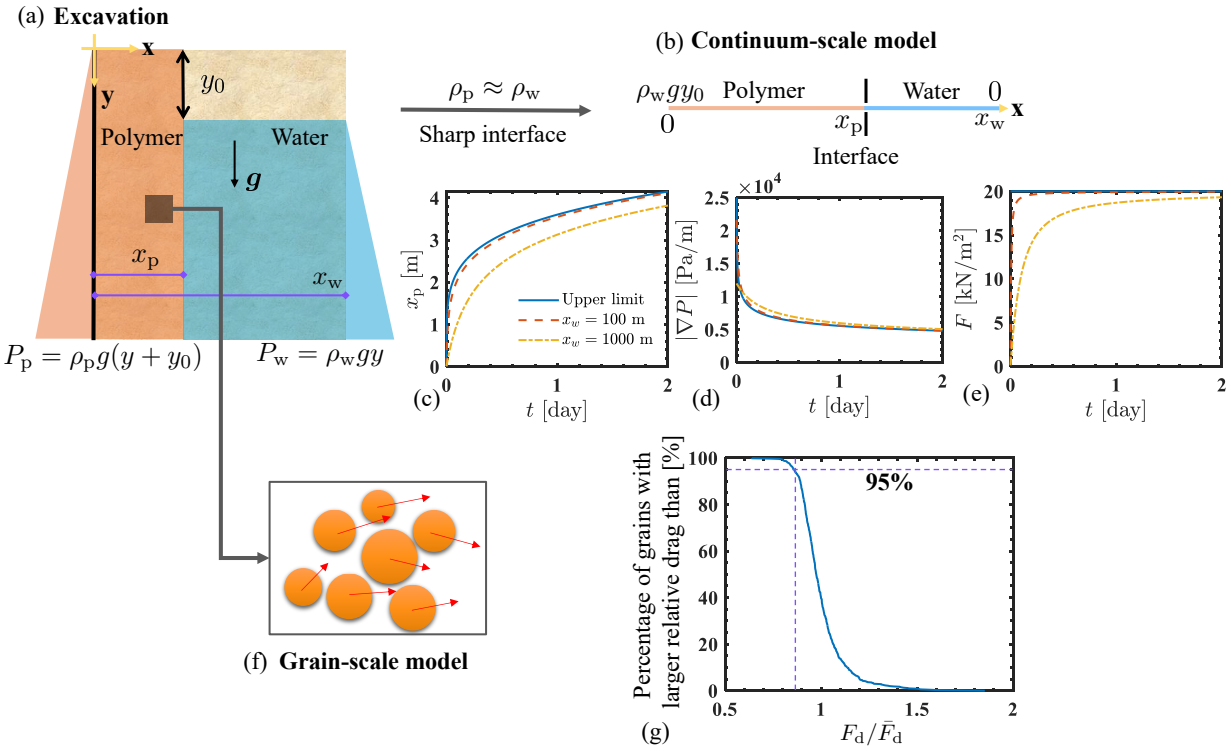


Fig. 11. (a) Schematic of an excavation with polymer permeating the surrounding soil where $y0$ is the head difference between water and polymer phases. (b) 1D continuum-scale model. Dynamics of (c) the polymer front, (d) the pressure gradient and (e) the total support force in the polymer phase for sand Ejezie A (LBS) with PHPA12 at different boundary conditions. (f) Zoomed-in schematic of grains with flow-induced drag forces. (g) Passing percentage of grains with larger $\tilde{F}_d$.